https://doi.org/10.48048/tis.2024.8762

Hydrophobic and Optical Properties of P(VDF-HFP) Nanofiber Filled with Nickel (II) Chloride Hexahydrate for Dye-Sensitized Solar Cells Application

Nikruesong Tohluebaji[1], Ratchanewan Siri[2], Nantakan Muensit[2], Chatchai Putson[2], Phongpichit Channuie[3], Paweena Porrawatkul[4] and Jureeporn Yuennan[4,*]

[1] *Faculty of Science and Technology, Princess of Naradhiwas University, Narathiwat 96000, Thailand*

[2] *Division of Physical Science (Physics), Faculty of Science, Prince of Songkla University, Songkhla 90112, Thailand*

[3] *School of Science, Walailak University, Thasala, Nakhon Si Thammarat 80160, Thailand*

[4] *Faculty of Science and Technology, Nakhon Si Thammarat Rajabhat University, Nakhon Si Thammarat 80280, Thailand*

([*] Corresponding author's e-mail: jureeporn_yue@nstru.ac.th)

Received: 29 July 2024, *Revised: 8 August 2024*, *Accepted: 13 August 2024*, *Published: 20 August 2024*

Abstract

This study explores the enhancement of dye-sensitized solar cells (DSSCs) by incorporating nickel chloride hexahydrate ($NiCl_2 \cdot 6H_2O$) into poly(vinylidene fluoride hexafluoropropylene) (P(VDF-HFP)) nanofiber mats. The addition of $NiCl_2 \cdot 6H_2O$ significantly improves the nanofiber morphology, leading to smoother, bead-free fibers with reduced diameters. Enhanced hydrophobicity is achieved through increased water contact angles and lower surface energy. Crystallinity and mechanical properties, including tensile stress and Young's modulus, are also improved, though ductility is reduced. Optical properties benefit from additional absorbance features due to Ni^{2+} ions, while electrical conductivity increases, forming conductive pathways that facilitate electron transport. These modifications collectively suggest that $NiCl_2 \cdot 6H_2O$/P(VDF-HFP) composite nanofibers can substantially improve DSSC performance by offering superior mechanical strength, hydrophobicity, and electrical conductivity.

Keywords: P(VDF-HFP), $NiCl_2 \cdot 6H_2O$, Hydrophobicity, Optical properties, dye-sensitized solar cells

1 Introduction

Solar cells are devices that harness energy from the sun by converting solar radiation directly into electricity. Conventional solar cells, primarily silicon-based, can achieve efficiencies as high as 30% under concentrated light [1, 2]. However, the high manufacturing cost limits the widespread adoption of silicon cells [3, 4, 5]. Dye-sensitized solar cells (DSSCs) have garnered significant attention due to their low cost, ease of fabrication, and environmental friendliness, making them a promising alternative to silicon solar cells [6, 7, 8]. DSSCs fabricated with conventional liquid electrolytes, typically comprising a triiodide/iodide redox couple in an organic solvent, have shown impressive energy conversion efficiencies [9, 10]. However, several drawbacks, such as the volatility of the electrolyte, difficulty in achieving robust sealing, liquid leakage, electrode corrosion, and dye photodecomposition, hinder their large-scale practical applications [11]. Consequently, many studies are focused on replacing liquid electrolytes with alternatives such as inorganic or organic hole conductors, ionic liquids, solid electrolytes, and polymer gel electrolytes [12].

Recent research indicates that DSSCs based on the polymer gel electrolytes, created by trapping a solution electrolyte within a three-dimensional matrix of polymer nanofibers, offer high conversion efficiencies similar to those of their liquid counterparts while maintaining good dimensional stability. In these nanofiber-based gel electrolytes, the liquid electrolyte is 'entrapped' within the host polymer matrix [13, 14]. There are numerous methods for producing polymer nanofibers, including drawing, template synthesis, phase separation, self-assembly, chemical vapor deposition, wet chemical synthesis, and electrospinning [15]. However, the applicability of most methods is limited by material type, cost, and production rate. Physical approaches such as electrospinning are advantageous due to their ability to produce consistent fibers with versatility, simplicity, low cost, and relatively high production rates [16, 17]. Electrospinning, a modification of the electrospraying process, relies on repulsive electrostatic forces to fabricate ultrafine nanofibers from polymer solutions or polymer melts [18, 19]. These fibers exhibit almost liquid-like ionic conductivities while offering better mechanical and chemical stability for DSSCs.

Among polymers used in electrochemical devices, P(VDF-HFP) stands out as a polymer matrix material for DSSCs due to its photoelectrochemical stability under potential application [4, 20, 21]. The presence of fluorine, which has a small ionic radius and high electronegativity, in P(VDF-HFP) is expected to improve ionic transport and reduce recombination rates at the semiconductor-polymer electrolyte interface in DSSCs. Additionally, PVDF-HFP is photochemically stable, making it a suitable electrolyte for long-term stability in DSSC appli-

cations. With a high dielectric constant of $\varepsilon = 8.4$, P(VDF-HFP) aids in the better dissociation of ionic salts [22, 23, 24]. P(VDF-HFP) consists of crystalline VDF, providing mechanical strength, and amorphous HFP, which entraps the liquid electrolyte. Even in the presence of HFP, the ionic conductivity of P(VDF-HFP) is about $10^{-8} - 10^{-10}$ S/cm [25, 26]. As reported, the DSSCs fabricated with P(VDF-HFP) nanofiber based gel electrolyte showed an energy conversion efficiency of 5.36% under 1.5 a.m. solar irradiation, whereas the efficiency of the DSSC made with the liquid electrolyte based cell was 6.01%. This shows the possibility of replacing the liquid electrolyte in DSSCs by electrospun polymer nanofiber based gel electrolyte and thereby minimizing some major drawbacks associated with liquid electrolyte based solar cells while maintaining a reasonably high efficiency [27]. Incorporating nanofillers into P(VDF-HFP) electrolyte can enhance properties governing DSSC performance, including materials such as TiO_2, SiO_2, ZnO, SnO_2, and ZrO_2 [28, 29, 30, 31]. The interfacial resistance of each interface (photoanode/electrolyte/counter electrode) in DSSCs plays a crucial role in photo conversion efficiency. Previous research investigated the electrical properties of P(VDF-HFP) composite films filled with nickel (II) chloride hexahydrate ($NiCl_2 \cdot 6H_2O$), revealing a microporous surface and enhanced conductivity, as well as uniform distribution of $NiCl_2 \cdot 6H_2O$. The water molecules within the salt are expected to interact with CF_2 groups of P(VDF-HFP) through hydrogen bond formation, enhancing compatibility between nanofillers and polymers [32].

The present study aims to develop solid-state dye-sensitized solar cells using $NiCl_2 \cdot 6H_2O$ in P(VDF-HFP) polymer electrolyte. Electrospun P(VDF-HFP) nanofiber mats were prepared using the electrospinning method. The effects of modified $NiCl_2 \cdot 6H_2O$ nanoparticles on the morphological, structural, mechanical, optical, and electrical properties of P(VDF-HFP) composite nanofibers were investigated to estimate their performance in DSSC applications.

2 Materials and methods

The copolymer used in this study was 10 wt% P(VDF-HFP) (Solef® 11010/1001; Solvay), with an average particle size of 100 - 120 μm, serving as the polymer matrix. Dimethylformamide (DMF, C_3H_7NO; AR1051-G4L; ACI Labscan), a highly polar solvent, was employed. Nickel (II) chloride hexahydrate ($NiCl_2 \cdot 6H_2O$; N6136) filler were purchased from Sigma-Aldrich. To prepare the electrospinning solution, P(VDF-HFP) powder was dissolved in a mixed solvent of DMF. The polymer concentration was maintained at 25 wt%. The solution was stirred at 50°C for 6 hours to ensure complete dissolution of the polymer. $NiCl_2 \cdot 6H_2O$ filler was then added to the polymer solution at varying concentrations (0.25 wt%, 0.5 wt%,

0.75 wt% and 1.0 wt%) to investigate the effect of Ni-salt loading on the properties of the nanofibers and the performance of the DSSCs. The mixture was stirred for an additional 3 hours to ensure uniform distribution of the $NiCl_2 \cdot 6H_2O$ within the polymer solution. The electrospinning equipment was set in horizontal baseline, consisted of a high-voltage power supply (Trek model 610E, USA), a syringe pump (Nz1000 NEWERA Pump Systems Inc., USA), and a collector covered with aluminum foil. The prepared solution was loaded into a 20 mL syringe equipped with a stainless-steel needle (gauge 20.5). The syringe pump was set to a flow rate of 0.5 mL/h. A voltage of 17 kV was applied between the needle tip and the collector, which was placed at 20 cm from the needle. The electrospinning process was conducted at room temperature with a relative humidity of 50-60%. The collected nanofibers were left to dry in a hot air oven at 60°C for 12 hours to remove any residual solvents.

3 Sample characterization

The surface morphology of the membranes was analyzed using scanning electron microscopy (SEM; FEI Quanta 400, Netherlands). The P(VDF-HFP) nanofiber mats were measured after gold sputtering under high vacuum at 20 kV. Elemental composition was determined using EDS integrated with SEM, focusing on carbon (C), fluorine (F), nickel (Ni), and chlorine (Cl), analyzed over three different areas per sample to calculate mean values. ImageJ software was used to analyzed average fiber diameter and porosity from SEM images. To understand the wettability and surface characteristics of the obtained nanofibers, the water contact angle (WCA) and surface energy (SE) were investigated using a Dataphysics contact angle system (OCA-15EC, Germany) in static sessile drop mode. A droplet of water was deposited on the nanofiber surface, and images were captured to analyze the contact angle formed by the droplet, indicating surface hydrophobicity. Using the captured data, SE was calculated using WU models to determine the dispersive and polar components of the surface energy. The crystal structures of the samples were examined using X-ray diffraction (XRD; X'Pert MPD, Philips, Netherlands) and Fourier transform infrared spectroscopy (FTIR; Vertex70, Bruker, Germany). XRD analysis was conducted at 40 kV and 30 mA using Cu-Kα radiation with a wavelength of 0.154 nm, at a scan rate of 3° min^{-1}. FTIR measurement was performed at room temperature in attenuated total reflectance (ATR) mode, ranging from 1600 to 400 cm-1 with a resolution of 2 cm^{-1}. To determine the mechanical properties, tensile testing measurements were conducted using a Zwick Roell Germany tensile testing machine (model z010) following the ISO 37-020 procedure. Five specimens were tested for each sample composition using a load cell of 100 N, with a deformation rate of 5 mm/min at room temperature. UV–Vis absorption and transmission studies were carried out using a

double-beam UV–Vis-NIR spectrometer (SPECORD 201 PLUS). Five specimens were cut to 2 × 2 cm^2 and put in a sample holder. The absorption and transmission were measured at 200–800 nm. Additionally, the ac conductivity of the fibers was conducted using an LCR meter (model IM 3533; HIOKI, Japan) as a function of frequency ranging from 1 Hz to 100 kHz at room temperature.

4 Results and discussion

4.1 Surface morphology

Figure 1 shows the SEM images of electrospun pure P(VDF-HFP) and $NiCl_2 \cdot 6H_2O$/P(VDF-HFP) nanofiber sheets at 1,000x and 10,000x magnification. Smooth and bead-free solid nanofibers are observed, arranged in a network with randomly oriented fibers. The scanned SEM images not only represent the morphology but also indicate the diameter distribution of the superfine fibers. However, the average fiber diameter and porosity of the nanofibers can be obtained by using the ImageJ analysis program to analyze the 1,000x and 10,000x SEM images, respectively. The average fiber diameter of the nanofibers was determined by collecting diameter measurements from multiple fibers to ensure accuracy. Then, the sum of all the diameter measurements was divided by the number of measurements to get the average fiber diameter. The porosity values were determined by contrasting the colors in the SEM image to identify the area of the fibers and the total area of the image. This tool allows setting the threshold values to differentiate between fibers and porous areas. If the fibers are black and the pores are white, the total area is the area of the entire image. The porosity can be determined using the formula [33]:

$$Porosity = \frac{Total\ area\ -\ Fiber\ area}{Total\ area} \times 100\%. \quad (1)$$

The average diameter and porosity values of the nanofibers are exhibited in Figure 2 and Table 1, respectively. For the pure P(VDF-HFP) nanofiber mat, the average diameter was 592.5 ± 10.1 nm. After adding the $NiCl_2 \cdot 6H_2O$ filler, a thinner diameter of $NiCl_2 \cdot 6H_2O$/P(VDF-HFP) composite nanofibers was obtained. The fiber diameter of the composite nanofibers gradually decreases with increasing $NiCl_2 \cdot 6H_2O$ content. This is due to the lower viscosity and higher ionic strength of the composite solution, which enhances fiber stretching and thinning during electrospinning, resulting in thinner fibers with potentially altered surface morphology and porosity [17, 34, 35].

The mean quantified elemental compositions obtained through SEM-EDS scans of electrospun pure P(VDF-HFP) and $NiCl_2 \cdot 6H_2O$/P(VDF-HFP) nanofiber mats are shown in Fig-

ures 3 and S1. For pure P(VDF-HFP), there are higher contents of F and C compared to the composite nanofibers. This is expected due to the chemical structure of P(VDF-HFP), which is a fluoropolymer [36, 37]. After adding $NiCl_2 \cdot 6H_2O$, the presence of Ni, Cl, and O is detected, originating from the $NiCl_2 \cdot 6H_2O$ component. The contents of F and C are reduced compared to pure P(VDF-HFP) due to the incorporation of $NiCl_2 \cdot 6H_2O$, which dilutes the original polymer content. It is evident that the introduction of $NiCl_2 \cdot 6H_2O$ to the P(VDF-HFP) matrix changes the overall elemental composition by introducing new elements (Ni, Cl, and O) and reducing the relative proportions of F and C. The well-interconnected structure formed by smooth nanofibers could increase the ability of the samples to trap the liquid electrolyte and facilitate the transport of ions in the inner space of the samples, which can effectively guarantee the high photoelectric conversion efficiency of the cells [38].

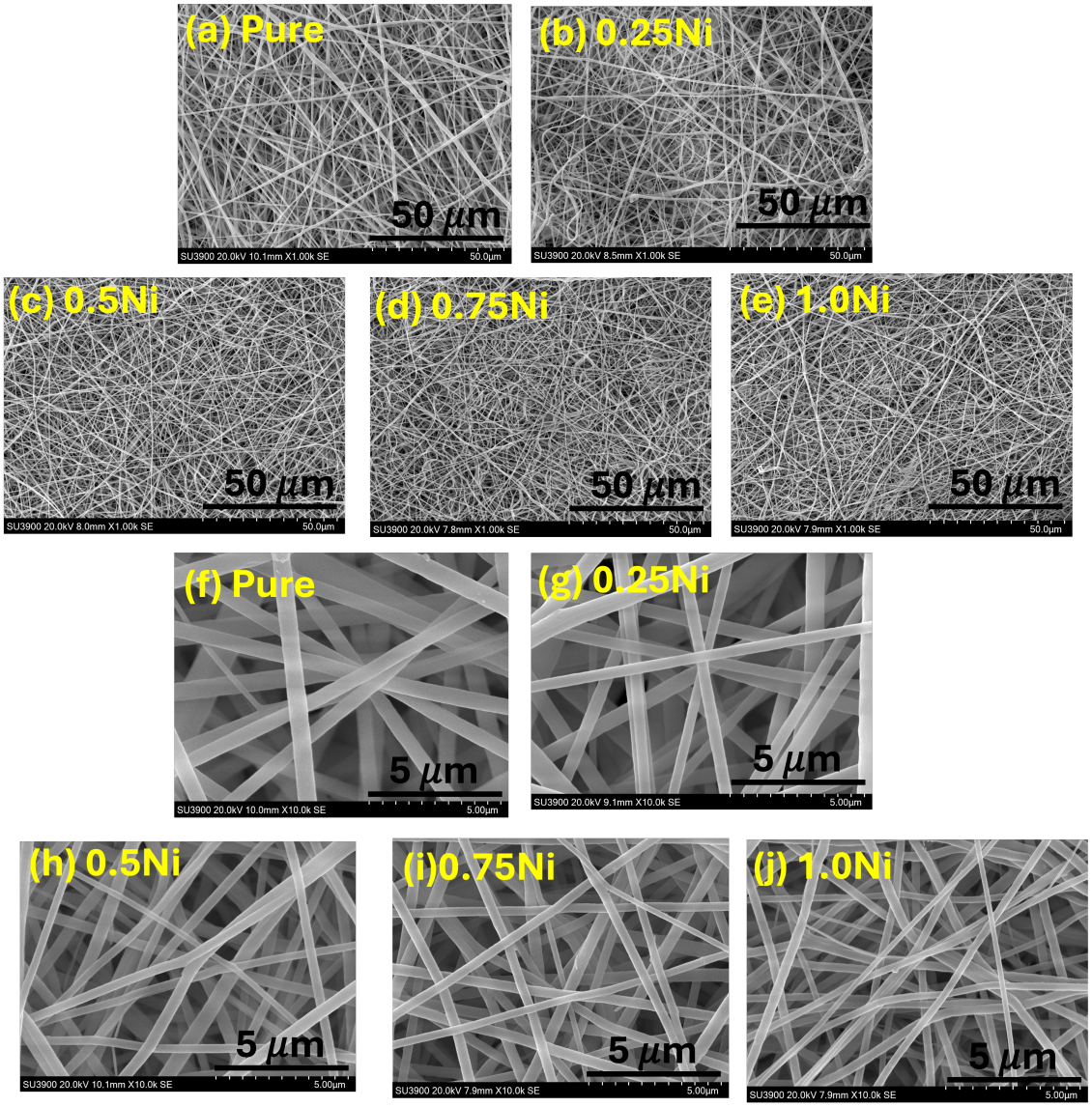

Figure 1: Scanned SEM images of electrospun pure P(VDF-HFP) and $NiCl_2 \cdot 6H_2O$/P(VDF-HFP) nanofiber mats with different $NiCl_2 \cdot 6H_2O$ concentrations at (a-e) x1,000 and (f-j) x10,000 magnifications.

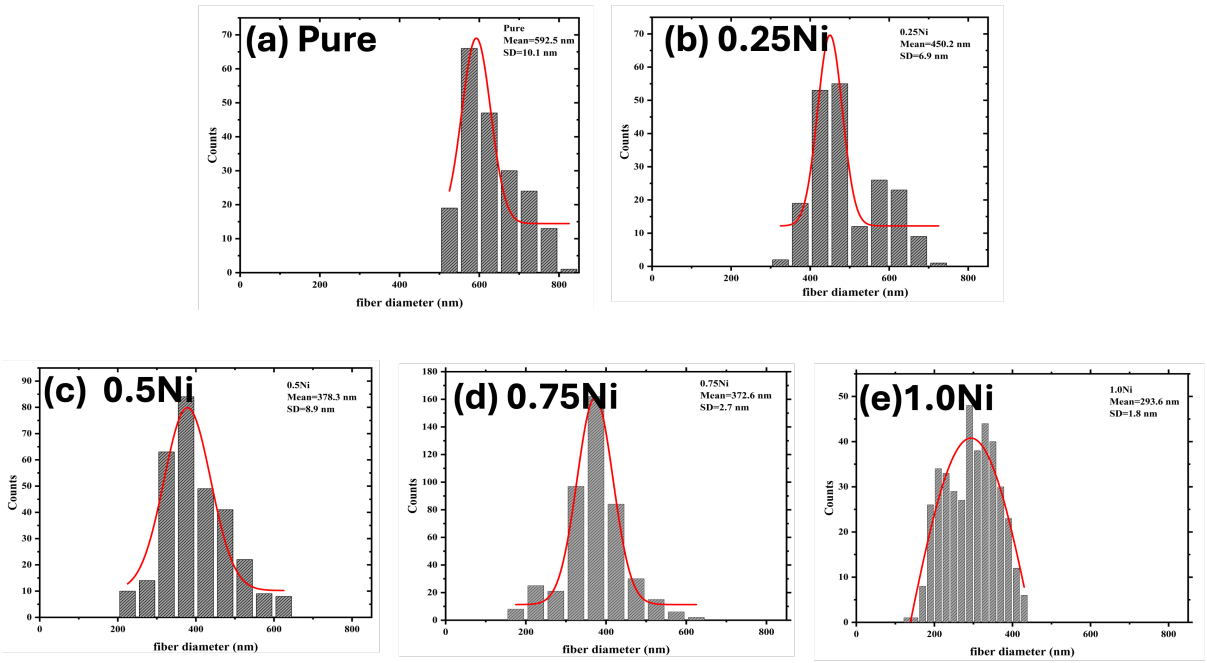

Figure 2: Evaluated average fiber diameter of electrospun pure P(VDF-HFP) and $NiCl_2 \cdot 6H_2O$/P(VDF-HFP) nanofiber mats with different $NiCl_2 \cdot 6H_2O$ concentrations by ImageJ software.

Table 1: Average fiber diameter, porosity, average water contact angle, and average surface energy of electrospun pure P(VDF-HFP) and $NiCl_2 \cdot 6H_2O$/P(VDF-HFP) nanofiber mats with different $NiCl_2 \cdot 6H_2O$ concentrations

P(VDF-HFP) nanofiber	**Average fiber diameter** (nm)	**Porosity** (%)	**Average water contact angle** (°)	**Average surface energy** (mJ/m^2)
Pure	592.5 ± 10.1	58.71	132.19 ± 3.85	15.43 ± 0.70
0.25%Ni	450.2 ± 6.9	49.73	132.93 ± 1.53	10.85 ± 0.60
0.50%Ni	378.3 ± 8.9	48.79	138.74 ± 0.97	10.77 ± 0.33
0.75%Ni	372.6 ± 2.5	45.62	139.65 ± 1.95	10.61 ± 0.45
1.00%Ni	293.6 ± 1.8	44.72	141.88 ± 2.61	10.28 ± 0.58

4.2 Water contact angle

The water contact angle (WCA) and surface energy (SE) were examined to assess the wetting properties of the nanofiber mat surfaces. For each nanofibrous sample, the WCA and SE values were measured in three areas and then averaged. Typically, P(VDF-HFP) nanofibers form a rough surface with low SE substances; if the WCA is more than 90°, the surface is considered hydrophobic, and if it exceeds 150°, it is deemed superhydrophobic, particularly due to the presence of fluoropolymers [39, 40]. Table 1 and Figure 4 show the WCA and SE values of electrospun pure P(VDF-HFP) and $NiCl_2 \cdot 6H_2O$/P(VDF-HFP) nanofiber mats, respectively. The results indicate that all the prepared electrospun nanofibers exhibit WCA values ranging from 132.19° ± 3.85° to 141.88° ± 2.61°, which are indicative of significantly hydrophobic surfaces. The WCA of the pristine P(VDF-HFP) nanofiber was measured

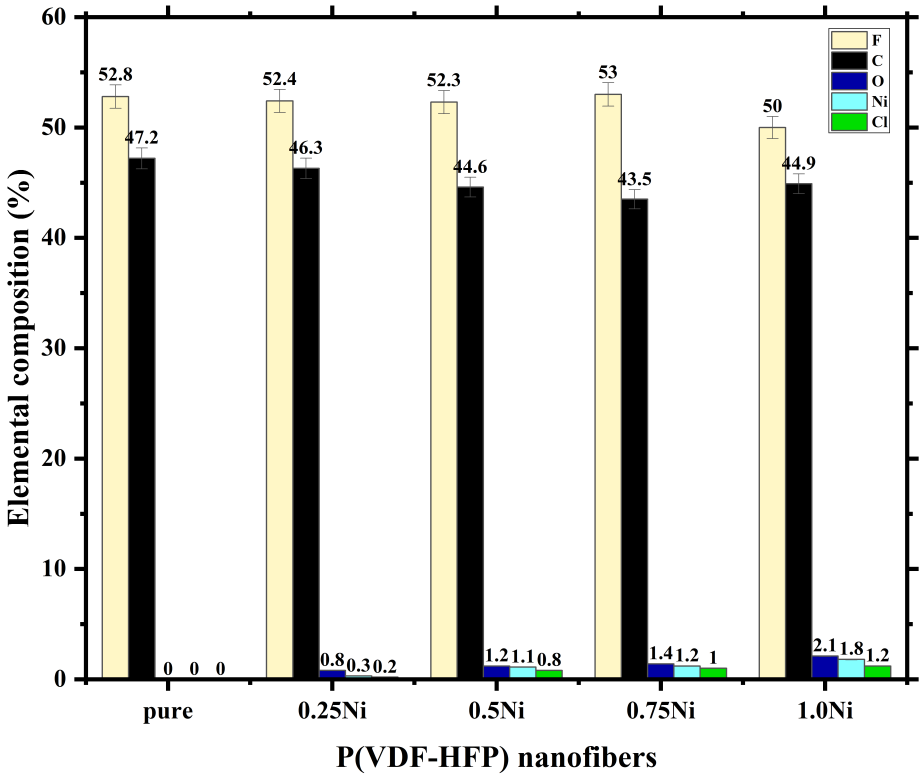

Figure 3: Elemental composition of electrospun pure P(VDF-HFP) and $NiCl_2 \cdot 6H_2O$/P(VDF-HFP) nanofiber mats with different $NiCl_2 \cdot 6H_2O$ concentrations measured through SEM-EDS at x1,000 magnification.

to be 132.19° ± 3.85°, consistent with previous studies that reported similar WCA values for pure electrospun P(VDF-HFP) membranes [41].

The hydrophobicity of the composite nanofibers was enhanced due to the incorporation of $NiCl_2 \cdot 6H_2O$, which resulted in a lower SE. The 1.0% $NiCl_2 \cdot 6H_2O$/P(VDF-HFP) nanofiber sheet exhibited average WCA and SE values of 141.88° ± 2.61° and 10.28 ± 0.58 mJ/m², respectively. A lower SE indicates that the P(VDF-HFP) surface has less affinity for water, causing water molecules to form droplets rather than spreading out, thereby increasing the contact angle [42]. In the case of P(VDF-HFP) nanofibers with added $NiCl_2 \cdot 6H_2O$, the SE is further reduced, along with a decrease in fiber diameter. Consequently, the randomly thinner P(VDF-HFP) nanofibers without beads create a rougher surface texture, which presents a high WCA as explained by Nuamcharoen and coauthor [43]. The wetting phenomena were explained by the contact radii of the water droplets on the surface of P(VDF-HFP) sheets, determined as a function of surface roughness [44]. This roughness can trap air, leading to the Cassie-Baxter state, where the water droplet sits on a composite surface of air and solid, further increasing the WCA. The increased WCA can be described by the Cassie-Baxter

model [40, 45]:

$$\cos\theta^c = f(1+\cos\theta) - 1\,, \tag{2}$$

where θ^c is the apparent contact angle, θ is the intrinsic contact angle, and f is the solid fraction, which is related to surface roughness. These findings clearly demonstrate that the nanofibrous films can create a hierarchical micro/nanostructure surface, efficiently trapping more air bubbles, the increased WCA values also contributed to improve of hydrophobicity, which can enhance the anti-wetting property [41, 46].

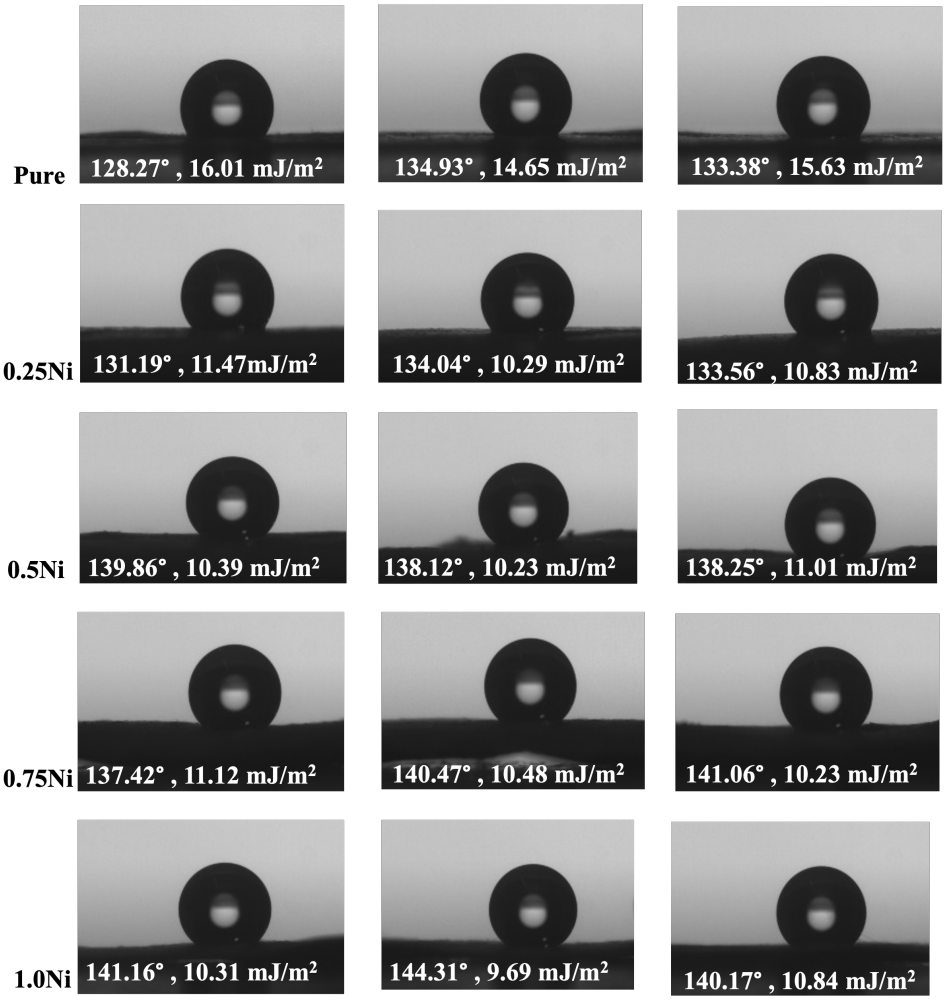

Figure 4: Water contact angle and surface energy in 3 areas of pure P(VDF-HFP) and $NiCl_2{\cdot}6H_2O$/P(VDF-HFP) nanofiber mats with different $NiCl_2{\cdot}6H_2O$ concentrations.

4.3 Crystal structure

Figure 5 presents the XRD profiles used to determine the crystallite size and structure of pristine P(VDF-HFP) and $NiCl_2{\cdot}6H_2O$/P(VDF-HFP) nanofiber mats with varying concentrations of $NiCl_2{\cdot}6H_2O$. The XRD pattern of pure P(VDF-HFP) nanofibers displayed character-

istic peaks at 18.4° and 20.1°, corresponding to the (020) and (110) planes of P(VDF-HFP) crystals, respectively. This confirms partial crystallization and indicates a semicrystalline structure of P(VDF-HFP) [47, 48]. A similar pattern was observed when $NiCl_2 \cdot 6H_2O$ was incorporated into the polymer matrix. However, the peaks at 36.4° (311) and 57.6° (206) showed gradual growth with increasing $NiCl_2 \cdot 6H_2O$ concentrations, indicating the presence of intrinsic $NiCl_2 \cdot 6H_2O$ nanofillers. The crystallite size (D) was estimated using the Scherrer Equation [49, 50]:

$$D = k\lambda/\beta \cos\theta, \tag{3}$$

where k is the Scherrer constant (0.89), λ is the X-ray wavelength corresponding to Cu-Kα irradiation (0.154 nm), β is the full width at half maximum (FWHM) of the peak (in radians), and θ is the diffraction angle (in degrees). Crystallinity was also calculated using the equation [51]:

$$X_c = \frac{\sum A_{cr}}{\sum A_{cr} + \sum A_{amr}} \times 100\,, \tag{4}$$

where A_{cr} and A_{amr} are the total integrated areas of the crystalline diffraction peaks and the amorphous halo, respectively. Table 2 shows the crystallite size and crystallinity of pristine P(VDF-HFP) and $NiCl_2 \cdot 6H_2O$/P(VDF-HFP) nanofiber mats. It was found that both crystallite size and crystallinity increased with the addition of $NiCl_2 \cdot 6H_2O$. The modification was more pronounced with higher amounts of $NiCl_2 \cdot 6H_2O$, indicating that the crystalline domains within the polymer matrix grew larger. $NiCl_2 \cdot 6H_2O$ can interact with the P(VDF-HFP) matrix, reducing the mobility of the polymer chains. This reduction in mobility can lead to more orderly and larger crystalline structures as the polymer chains are less able to interfere with the growing crystals. However, the maximum value of crystallinity obtained at 1.0 wt% $NiCl_2 \cdot 6H_2O$/P(VDF-HFP) nanofiber mat is little increased by 2.7% compared with the pure P(PVDF-HFP). These blended materials exhibited the inherent semi-crystalline phase nature of the polymers [52, 53, 54]. This small enhancement can be attributed to the interaction between $NiCl_2 \cdot 6H_2O$ and the P(VDF-HFP) matrix.

FTIR analysis was conducted on both pristine P(VDF-HFP) and $NiCl_2 \cdot 6H_2O$/P(VDF-HFP) nanofiber mats to further explore the crystal structure induced by different $NiCl_2 \cdot 6H_2O$ contents. Figure 6 presents the FTIR patterns for all electrospun P(VDF-HFP) films. The intense vibrational bands at 482 cm^{-1} (CF_2 bending and wagging), 510 cm^{-1} (CF_2 bending), 617 and 765 cm^{-1} (mixed CF_2 bending and CCC skeletal vibration), 840 cm^{-1} (mixed CH_2 rocking and CF_2 asymmetric stretching), 881 cm^{-1} (mixed CH_2 rocking and CF_2 bending), 1,075 cm^{-1} (CF_3 out-of-plane deformation), 1,176 cm^{-1} (CF_2 antisymmetric stretching), 1,275 and 1,400 cm^{-1} (CH_2 wagging), and 1,453 cm^{-1} (in-plane bending or scissoring) are

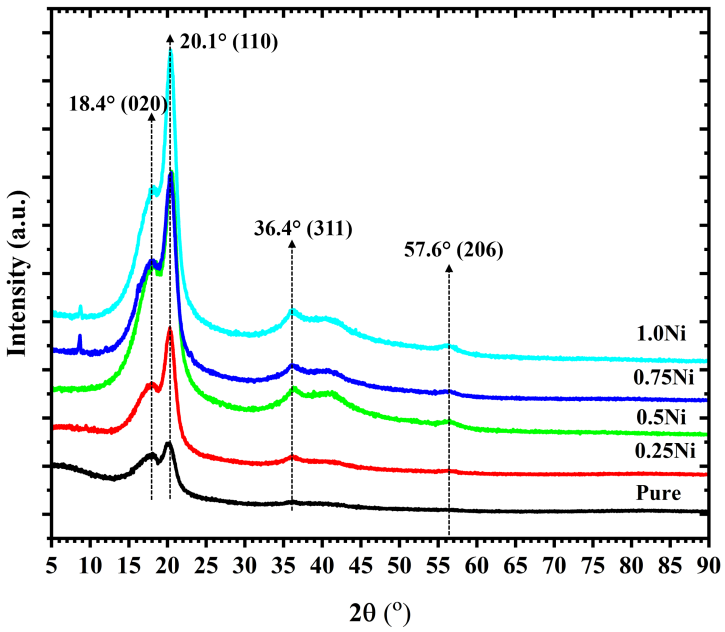

Figure 5: XRD profiles used to determine the crystallite size and structure of pristine P(VDF-HFP) and $NiCl_2 \cdot 6H_2O$/P(VDF-HFP) nanofiber mats with varying concentrations of $NiCl_2 \cdot 6H_2O$.

evident for all nanofibers [59, 60]. These peaks may be related to interchain interactions within the P(VDF-HFP) polymer [61].

As seen from the FTIR patterns, the $NiCl_2 \cdot 6H_2O$/P(VDF-HFP) nanofiber mats also show a peak around 475 cm^{-1}, which is not visible in the pure P(VDF-HFP). This peak can be associated with interactions involving both the P(VDF-HFP) polymer and the $NiCl_2 \cdot 6H_2O$ filler. For P(VDF-HFP), the band around 475 cm^{-1} is typically associated with the deformation or bending vibrations of the CF_2 groups within the polymer chain [62]. For $NiCl_2 \cdot 6H_2O$, this band can correspond to the Ni-Cl stretching vibrations, as metal-halide stretching vibrations generally appear in the lower wavenumber region of the IR spectrum. When $NiCl_2 \cdot 6H_2O$ is incorporated into the P(VDF-HFP) film, the Ni^{2+} ions from $NiCl_2 \cdot 6H_2O$ can coordinate with the polymer matrix, potentially altering the local electronic environment of the CF_2 groups and causing shifts or changes in the intensity of their deformation or bending vibrations. Additionally, the water molecules in $NiCl_2 \cdot 6H_2O$ can form hydrogen bonds with the polymer chains, influencing the vibrational modes of the polymer, particularly the CF_2 groups, leading to modifications in the FTIR spectrum. Furthermore, the band at 475 cm^{-1} may represent overlapping vibrational contributions from both the CF_2 bending vibrations in PVDF-HFP and the Ni-Cl stretching vibrations in $NiCl_2 \cdot 6H_2O$. The presence of both components in the composite can result in a combined vibrational mode that appears at this wavenum-

ber. Thus, these interactions collectively influence the vibrational characteristics observed at this wavenumber, providing insights into the molecular dynamics within the composite nanofibers.

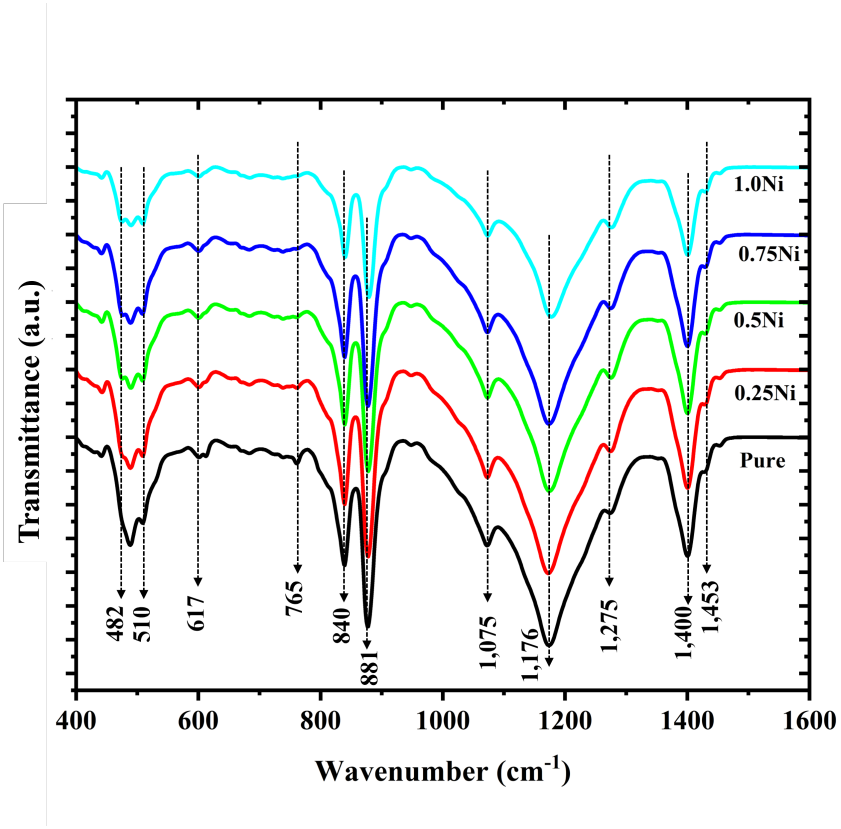

Figure 6: FTIR patterns of pristine P(VDF-HFP) and $NiCl_2 \cdot 6H_2O$/P(VDF-HFP) nanofiber mats with varying concentrations of $NiCl_2 \cdot 6H_2O$.

Table 2: Crystallite size, Crystallinity, of electrospun pure P(VDF-HFP) and $NiCl_2 \cdot 6H_2O$/P(VDF-HFP) nanofiber mats with different $NiCl_2 \cdot 6H_2O$ concentrations.

P(VDF-HFP) nanofiber	**FWHM** (rad)	**crystallite size** (nm)	**Crystallinity** (%)
Pure	0.6240	13.0	59.73
0.25%Ni	0.3120	25.9	60.13
0.50%Ni	0.3582	38.7	60.49
0.75%Ni	0.3070	45.1	61.03
1.00%Ni	0.2047	68.2	61.37

4.4 Mechanical properties

Figure 7 and Table 3 respectively show the stress-strain curves and mechanical properties of the electrospun P(VDF-HFP) nanofibers. To determine the maximum tensile stress, Young's modulus, and elongation at break from a stress-strain curve, we first identify the maximum tensile stress as the highest stress a material can withstand while being stretched before it breaks, obtained from the peak of the stress-strain curve. Young's modulus (E), or the elastic modulus, is determined from the initial linear portion of the stress-strain curve,

where the material behaves elastically, by calculating the slope (E = stress/strain). Elongation at break is the strain value at which the material breaks, measuring its ductility and representing the extent to which the material can be stretched or elongated before it breaks, expressed as a percentage of the original length [63, 64, 65].

The observed data show that the maximum tensile stress, Young's modulus, and elongation at break of P(VDF-HFP) nanofibers are significantly influenced by the incorporation of $NiCl_2 \cdot 6H_2O$ nanofibers. Compared to pure P(VDF-HFP), the composite nanofibers exhibit higher maximum tensile stress and Young's modulus values, increasing from 4.19 MPa to 6.20 MPa and from 47.82 kPa to 102.40 kPa, respectively, with the addition of $NiCl_2 \cdot 6H_2O$. This indicates that the composite nanofibers have a more rigid structure, making them capable of withstanding greater stress before failure. However, the elongation at break decreases from 133% (pure) to 62% (with 1.00% Ni), indicating that the material becomes less ductile and more brittle with higher concentrations of $NiCl_2 \cdot 6H_2O$ nanofibers. The most notable decrease in ductility occurs as the concentration reaches 0.75% Ni and above. Thus, incorporating $NiCl_2 \cdot 6H_2O$ nanofibers into PVDF-HFP nanofibers results in a trade-off between enhanced strength and stiffness and reduced ductility [38]. The optimal concentration of nanofibers depends on the specific application requirements, balancing the need for mechanical strength and stiffness against the desired level of flexibility and ductility. For applications requiring high strength and rigidity, higher concentrations of $NiCl_2 \cdot 6H_2O$ nanofibers (0.75% to 1.00% Ni) are beneficial. However, for applications where some level of ductility is needed, lower concentrations (0.25% to 0.50%) might be more appropriate.

Table 3: Maximum tensile stress, Young's modulus, and Elongation at break of electrospun pure P(VDF-HFP) and $NiCl_2 \cdot 6H_2O$/P(VDF-HFP) nanofiber mats with different $NiCl_2 \cdot 6H_2O$ concentrations.

P(VDF-HFP) nanofiber	**Maximum tensile stress** (MPa)	**Young's modulus** (kPa)	**Elongation at break** (%)
Pure	3.35	38.25	133
0.25%Ni	4.19	47.82	125
0.50%Ni	4.24	48.55	107
0.75%Ni	5.17	78.52	67
1.00%Ni	6.20	102.40	62

4.5 Optical properties

To measure the absorption spectrum of the fibers and identify the wavelengths at which they absorb light, we recorded the UV-Vis spectra, which are crucial for understanding the interaction of the fibers with light for DSSC applications. Optical absorption spectra of electrospun pure P(VDF-HFP) and $NiCl_2 \cdot 6H_2O$/P(VDF-HFP) nanofiber mats with varying $NiCl_2 \cdot 6H_2O$ concentrations were obtained at room temperature using a UV-Vis spectrome-

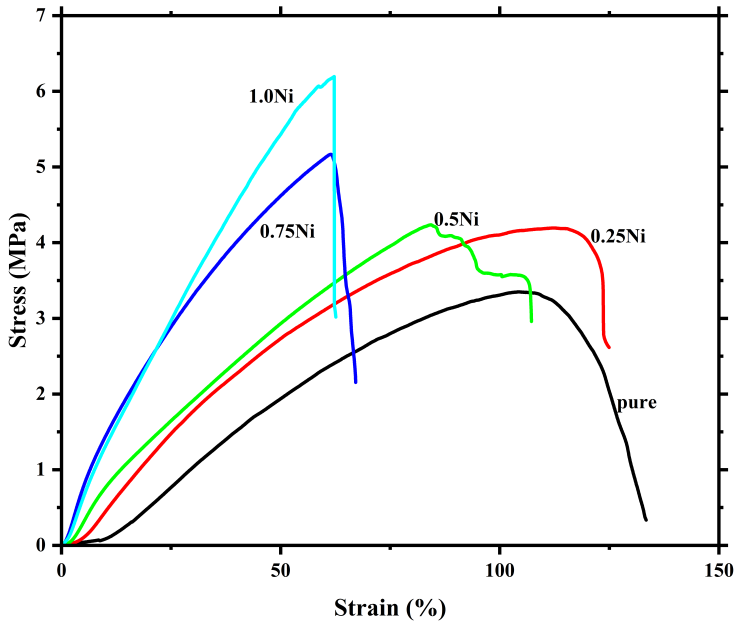

Figure 7: Stress-strain curves of pristine P(VDF-HFP) and $NiCl_2 \cdot 6H_2O$/ P(VDF-HFP) nanofiber mats with varying concentrations of $NiCl_2 \cdot 6H_2O$.

ter over the range of 200–800 nm, as shown in Figure 7. Similar UV-Vis absorbance trends were observed between pure P(VDF-HFP) fibers and $NiCl_2 \cdot 6H_2O$/P(VDF-HFP) composite nanofibers in the broad band at 281-318 nm. For pure P(VDF-HFP) nanofibers, the absorbance in this range can be attributed to intrinsic electronic transitions. When $NiCl_2 \cdot 6H_2O$ is added, the composite nanofibers exhibit additional absorbance features primarily due to the transitions of Ni^{2+} ions (0.069 nm) and charge transfer transitions between Ni^{2+} and its ligands [55]. However, the overall absorbance trend remains similar because the dominant absorbing species in this range is the P(VDF-HFP) polymer. Thus, the broad band at 281-318 nm observed in both pure P(VDF-HFP) and $NiCl_2 \cdot 6H_2O$/P(VDF-HFP) composite nanofibers is primarily due to the intrinsic electronic transitions of the P(VDF-HFP) polymer. These transitions dominate the absorbance in this range, resulting in similar trends between pure and composite nanofibers. The addition of $NiCl_2 \cdot 6H_2O$ introduces new absorbance features, but the fundamental polymer absorbance properties still largely dictate the observed spectrum in this range. It is well-known that analyzing the fundamental absorption edge provides crucial information about the optical band gap. An absorption edge occurs when a photon excites an electron during the absorption process, moving it from a lower to a higher energy state. The optical band gap energy (E_g) is estimated using the following relation [56]:

$$\alpha h\nu = B(h\nu - E_g)^{1/2}, \quad (5)$$

where α is the absorption coefficient and equals to 2.303 (absorbance)/(thickness of the film), B is constant, and h is the photon energy. Figure 9 represents the relation between $(\alpha h\nu)^2$ against photon energy $h\nu$. The band gap energy is estimated from the intercept of the linear portion of the curve with zero $h\nu$ axis. As observed, the band gap energy of $NiCl_2 \cdot 6H_2O$/P(VDF-HFP) were gradually increased with increasing $NiCl_2 \cdot 6H_2O$ contents. This behavior may be associated with the structural changes occurring after addition of $NiCl_2 \cdot 6H_2O$. However, the maximum band gap energy of 3.24 eV obtained at 1.0 wt% $NiCl_2 \cdot 6H_2O$/P(VDF-HFP) nanofibers increased slightly by 0.14 eV compared to pure P(VDF-HFP). This value is also lower than that of the PVDF-HFP/$LiClO_4$ nanocomposite film, which has a band gap energy of 3.49 eV in the unirradiated state, as reported by Yesappa and co-workers [57]. which makes it useful for the electrical application.

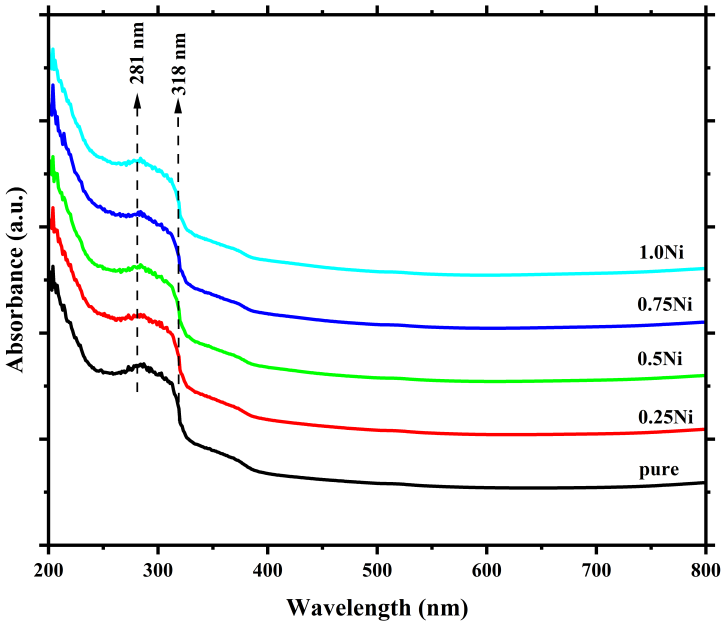

Figure 8: UV–VIS absorption spectra of pristine P(VDF-HFP) and $NiCl_2 \cdot 6H_2O$/P(VDF-HFP) nanofiber mats with varying concentrations of $NiCl_2 \cdot 6H_2O$.

4.6 Electrical properties

The AC conductivity of pristine P(VDF-HFP) and $NiCl_2 \cdot 6H_2O$/P(VDF-HFP) nanofiber mats as a function of frequency is shown in Figure 8. The AC conductivity varies with applied frequency and concentrations of $NiCl_2 \cdot 6H_2O$. The AC conductivity value (σ_{ac}) was calculated using the equation [66]:

$$\sigma_{ac} = \omega C_p d \tan\delta, \tag{6}$$

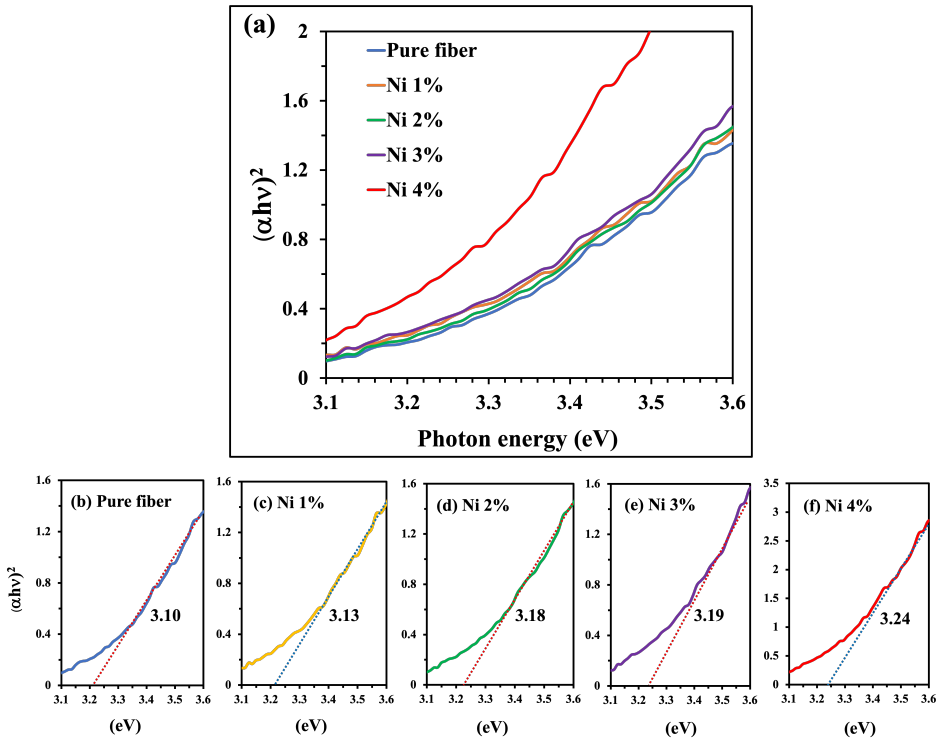

Figure 9: (a) The relation between $(\alpha h\nu)^2$ and $h\nu$ of pristine P(VDF-HFP) and $NiCl_2 \cdot 6H_2O$/P(VDF-HFP) nanofiber mats with varying concentrations of $NiCl_2 \cdot 6H_2O$ and (b-f) the insert spectrum of different P(VDF-HFP) samples.

where ω is angular frequency of the applied AC field, C_p is the measured capacitance value of the sample, d is the thickness of the sample, A is the electrode area, and $\tan\delta$ is the loss tangent or dissipation factor, which is the ratio of the imaginary part to the real part of the complex permittivity. It was found that the AC conductivity increases slightly with frequency as it approaches the resonance frequency of the charge carriers along the polymer chain [22]. AC conductivity is frequency-independent at lower frequencies due to the presence of free charges and becomes frequency-dependent at higher frequencies due to the release of activated trapped charges. Pristine P(VDF-HFP) nanofiber mats have initially low electrical conductivity, typical for pure polymeric materials, which generally lack conductive pathways. Adding $NiCl_2 \cdot 6H_2O$ to the P(VDF-HFP) matrix introduces conductive ions and potentially creates conductive pathways within the polymer matrix which agreed with the results for morphology and porosity. The electrical conductivity of the composite nanofiber mats increases with the concentration of $NiCl_2 \cdot 6H_2O$, as charge carriers are more easily transported along the polymer chain [67]. At low concentrations of $NiCl_2 \cdot 6H_2O$, there is a modest increase in conductivity compared to pristine P(VDF-HFP), indicating that even small amounts of $NiCl_2 \cdot 6H_2O$ can enhance the electrical properties. At higher concentrations, the conductivity continues to rise steadily, suggesting the formation of a percolating network of conductive pathways, where Ni^{2+} ions create continuous channels for charge transport across

the nanofiber mat. The homogeneous attachment of $NiCl_2 \cdot 6H_2O$ nanoparticles facilitates the segmental mobility of polymer chains, aiding in the dissociation of ions in the polymer matrix, thereby increasing the ionic conductivity of the composite nanofibers. This enhanced conductivity can improve electron transport and reduce recombination losses in dye-sensitized solar cells, potentially increasing their efficiency as reported by Dissanayake and co-worker [58].

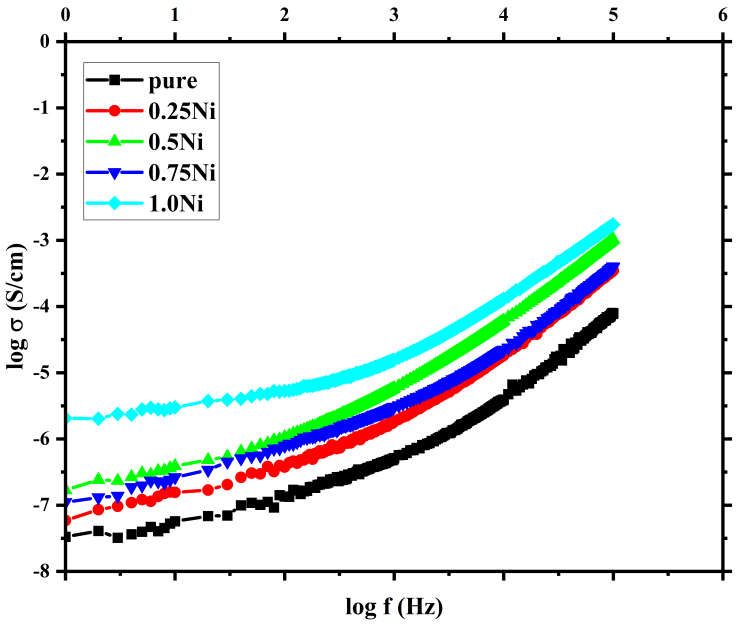

Figure 10: Ac conductivity of pristine P(VDF-HFP) and $NiCl_2 \cdot 6H_2O$/ P(VDF-HFP) nanofiber mats with varying concentrations of $NiCl_2 \cdot 6H_2O$.

5 Conclusions

This study investigates the integration of nickel chloride hexahydrate ($NiCl_2 \cdot 6H_2O$) into P(VDF-HFP) nanofiber mats to create composite materials with improved characteristics for DSSC applications. The incorporation of $NiCl_2 \cdot 6H_2O$ significantly modifies the morphology, hydrophobicity, crystallinity, and mechanical properties of the P(VDF-HFP) nanofiber mats. SEM analysis shows that the addition of $NiCl_2 \cdot 6H_2O$ results in smoother, bead-free fibers with reduced diameters, enhancing the overall surface morphology. The hydrophobicity of the nanofibers is markedly increased, as indicated by higher water contact angles and lower surface energy values, which is beneficial for DSSC performance due to better water repellency. XRD and FTIR analyses reveal that the crystallinity and molecular interactions within the polymer matrix are positively influenced by $NiCl_2 \cdot 6H_2O$, resulting in larger crystalline

domains and new vibrational features. Furthermore, the mechanical properties are significantly improved, with increases in maximum tensile stress and Young's modulus, albeit at the expense of reduced ductility. The optical properties are enhanced, as evidenced by additional UV-Vis absorbance features introduced by Ni^{2+} ions, while the electrical conductivity is substantially increased, facilitating better electron transport and reduced recombination losses. These enhancements collectively suggest that $NiCl_2 \cdot 6H_2O$/P(VDF-HFP) composite nanofibers are highly suitable for improving the efficiency and durability of DSSCs.

Acknowledgements

This work (grant no. RGNS 65-169) was financially supported by the office of the Permanent Secretary, Ministry of Higher Education, Science, Research and Innovation (OPS MHESI), Thailand Science Research and Innovation (TSRI). Additionally, the authors would like to thank Faculty of Science and Technology, Nakhon Si Thammarat Rajabhat University, Faculty of Science and Technology, Princess of Naradhiwas University, Division of Physical Science (Physics), Faculty of Science, Prince of Songkla University and Center of Excellence in Nanotechnology for Energy (CENE), Prince of Songkhla University for instrumental supports.

References

[1] AM Oni, ASM Mohsin, MM Rahman and MBH Bhuian. A comprehensive evaluation of solar cell technologies, associated loss mechanisms, and efficiency enhancement strategies for photovoltaic cells. *Energy Reports*, 2024; **11**, 3345-3366.

[2] MM Noor, MH Buraidah, SNF Yusuf, MA Careem, SR Majid and AK Arof. Performance of Dye-Sensitized Solar Cells with (PVDF-HFP)-KI-EC-PC Electrolyte and Different Dye Materials. *International Journal of Photoenergy*, 2011; **1**, 960487.

[3] D Zheng, X Yang, L Cucek, J Wang, T Ma and C Yin. Revolutionizing dye-sensitized solar cells with nanomaterials for enhanced photoelectric performance. *Journal of Cleaner Production*, 2024; **464**, 142717.

[4] JY Park, JW Lee, KH Park, TY Kim, SH Yim, XG Zhao, HB Gu and EM Jin. Dye-sensitized solar cells based on electrospun poly(vinylidenefluoride-co-hexafluoropropylene) nanofibers. *Polymer Bulletin*, 2013; **70 (2)**, 507-515.

[5] M Nazeeruddin, E Baranoff and M Grätzel. Dye-sensitized solar cells: A brief overview. *Solar Energy*, 2011; **85**, 1172-1178.

[6] H Iftikhar, GG Sonai, SG Hashmi, AF Nogueira and PD Lund. Progress on Electrolytes Development in Dye-Sensitized Solar Cells. *Materials (Basel)*, 2019; **12 (12)**, 1998.

[7] Masud and HK Kim. Redox Shuttle-Based Electrolytes for Dye-Sensitized Solar Cells: Comprehensive Guidance, Recent Progress, and Future Perspective. *ACS Omega*, 2023; **8 (7)**, 6139-6163.

[8] L Han, A Islam, H Chen, C Malapaka, B Chiranjeevi, S Zhang, X Yang and M Yanagida. High-efficiency dye-sensitized solar cell with a novel co-adsorbent. *Energy & Environmental Science*, 2012; **5 (3)**, 6057-6060.

[9] S Yun, JN Freitas, AF Nogueira, Y Wang, S Ahmad and ZS Wangl. Dye-sensitized solar cells employing polymers. *Progress in Polymer Science*, 2016; **59**, 1-40.

[10] G Boschloo and A Hagfeldt. Characteristics of the Iodide/Triiodide Redox Mediator in Dye-Sensitized Solar Cells. *Accounts of Chemical Research*, 2009; **42**, 1819-1826.

[11] AE Anitha and M Dotter. A Review on Liquid Electrolyte Stability Issues for Commercialization of Dye-Sensitized Solar Cells (DSSC). *Energies*, 2023; **16 (13)**, 5129.

[12] Y Man, P Jaumaux, Y Xu, Y Fei, X Mo, G Wang and X Zhou. Research development on electrolytes for magnesium-ion batteries. *Science Bulletin*, 2023; **68 (16)**, 1819-1842.

[13] MAKL Dissanayake, MSH Hettiarachchi, GKR Senadeera, JMKW Kumari, K Umair, TMWJ Bandara, I Albinsson, M Furlani, BE Mellander, NB Chaure and OI Olusola. High-efficiency dye-sensitized solar cells fabricated with electrospun PVdF-HFP polymer nanofibre-based gel electrolytes. *Bulletin of Materials Science*, 2023; **46 (2)**, 80.

[14] S Venkatesan, YY Chen, CY Chien, MH Tsai, H Teng and YL Lee. Composite electrolyte pastes for preparing sub-module dye sensitized solar cells. *Journal of Industrial and Engineering Chemistry*, 2022; **107**, 383-390.

[15] I Alghoraibi and S Alomari. Different Methods for Nanofiber Design and Fabrication. In: A Barhoum, M Bechelany and A Makhlouf (Eds). *Handbook of Nanofibers, Springer International Publishing, Cham*, 2018, p.1-46.

[16] R Abdulhussain, A Adebisi, BR Conway and K Asare-Addo. Electrospun nanofibers: Exploring process parameters, polymer selection, and recent applications in pharmaceuticals and drug delivery. *Journal of Drug Delivery Science and Technology*, 2023; **90**; 105156.

[17] M Ahmadi Bonakdar and D Rodrigue. Electrospinning: Processes, Structures, and Materials. *Macromol*, 2024; **4 (1)**, 58-103.

[18] J Xue, T Wu, Y Dai and Y Xia. Electrospinning and Electrospun Nanofibers: Methods, Materials, and Applications. *Chemical Reviews*, 2019; **119 (8)**, 5298-5415.

[19] Y Huang, Y Li, Y Zhang, H Yu and Z Tan. Near-Field Electrospinning: Progress and Applications. *The Journal of Physical Chemistry C*, 2017; **121 (16)**, 8663-8678.

[20] W Xiang, W Huang, U Bach and L Spiccia. Stable high efficiency dye-sensitized solar cells based on a cobalt polymer gel electrolyte. *Chemical Communications*, 2013; **49 (79)**, 8997-8999.

[21] D Saikia, CC Han and YW Chen-Yang. Influence of polymer concentration and dyes on photovoltaic performance of dye-sensitized solar cell with P(VdF-HFP)-based gel polymer electrolyte. *Journal of Power Sources*, 2008; **185 (1)**, 570-576.

[22] Y Laxmayyaguddi, N Mydur, AS Shankar, V Hebri, M Vandana, G Sanjeev and D Hundekal. Modified Thermal, Dielectric, and Electrical Conductivity of PVDF-HFP/ LiClO4 Polymer Electrolyte Films by 8 MeV Electron Beam Irradiation. *ACS Omega*, 2018; **3 (10)**, 14188-14200.

[23] D Mouraliraman, N Shaji, S Praveen, M Nanthagopal, CW Ho, MV Karthik, T Kim and CW Lee. Thermally Stable PVDF-HFP-Based Gel Polymer Electrolytes for High-Performance Lithium-Ion Batteries. *Nanomaterials (Basel)*, 2022; **12 (7)**, 1056.

[24] LP Teo, MH Buraidah and AK Arof. Development on Solid Polymer Electrolytes for Electrochemical Devices. *Molecules*, 2021; **26 (21)**, 6499.

[25] TWTYT Farish Irfal Saaid. PVdF-HFP Quasi-solid-state Electrolyte for Application in Dye-sensitized Solar Cells. *International Journal of Technology*, 2018; **9 (6)**, 291-319.

[26] S Borah and M Deka. Study of electrical and electrochemical properties of P(VdF-HFP)-MMT based nanocomposite gel polymer electrolytes for application in energy storage devices. *Materials Science and Engineering: B*, 2021; **263**, 114822.

[27] N Kusumawati, P Setiarso, AB Santoso, S Muslim, Q A'yun and MM Putri. Characterization of poly (vinylidene fluoride-co-hexafluoropropylene) (PVdF-HFP) nanofiber membrane based quasi solid electrolytes and their application in a dye sensitized solar cell. *Electrochimica Acta*, 2018; **266**, 276-283.

[28] S Rahman, A Haleem, M Siddiq, MK Hussain, S Qamar, S Hameed and M Waris. Research on dye sensitized solar cells: recent advancement toward the various constituents of dye sensitized solar cells for efficiency enhancement and future prospects. *RSC Advances*, 2023; **13 (28)**, 19508-19529.

[29] M Ravi, KK Kumar, VM Mohan and VVRN Rao. Effect of nano TiO2 filler on the structural and electrical properties of PVP based polymer electrolyte films. *Polymer Testing*, 2014; **33**, 152-160.

[30] K Prabakaran, S Mohanty and SK Nayak. Improved electrochemical and photovoltaic performance of dye sensitized solar cells based on PEO/PVDF–HFP/silane modified TiO2 electrolytes and MWCNT/Nafion® counter electrode. *RSC Advances*, 2015; bf 5 (51), 40491-40504.

[31] S Dani, PN Channabasavanna, S Kulkarni, SR Manohara and K Udayakumar. The Electromagnetic Interference Shielding Effectiveness and Dielectric Response of PVDF-nTiO2Nanocomposites Thin Films. *Trends in Sciences*, 2022; **19 (21)**, 3046.

[32] P Sukwisute, J Yuennan and N Muensit. Enhancement of ferroelectric phase and dielectric properties of P(VDF-HFP) by NiCl2□6H2O nucleating agent. *Integrated Ferroelectrics*, 2019; **195 (1)**, 230-239.

[33] NH Astuti, NA Wibowo and MRSSN Ayub. The Porosity Calculation of Various Types of Paper Using Image Analysis. *Jurnal Pendidikan Fisika Indonesia*, 2018; **14 (1)**, 6.

[34] TJ Sill and HA von Recum. Electrospinning: Applications in drug delivery and tissue engineering. *Biomaterials*, 2008; **29 (13)**, 1989-2006.

[35] C Drew, X Wang, LA Samuelson and J Kumar. The Effect of Viscosity and Filler on Electrospun Fiber Morphology. *Journal of Macromolecular Science, Part A*, 2003; **40 (12)**, 1415-1422.

[36] N Tohluebaji, J Yuennan, Ci Putson and N Muensit. Improved Electroactive β Phase Nucleation and Dielectric Properties of P(VDF-HFP) Composite with Al(NO3)3·9H2O Fillers. *Integrated Ferroelectrics*, 2022; **224 (1)**, 181-191.

[37] G Magdy, AH Hassanin, I Kandas and N Shehata. PVDF Nanostructures Characterizations and Techniques for Enhanced Piezoelectric Response: A Review. *Materials Chemistry and Physics*, 2024; **325**, 129760.

[38] F Cheng, Y Ou, G Liu and L Zhao. Binghai Dong, Shimin Wang, Novel Quasi-Solid-State Electrolytes based on Electrospun Poly(vinylidene fluoride) Fiber Membranes for Highly Efficient and Stable Dye-Sensitized Solar Cells. *Nanomaterials*, 2019; **9 (5)**, 783.

[39] J Yuennan, S Nawae, N Tohluebaji, C Putson and N Muensit, Preparation of super-hydrophobic surface on P(VDF-HFP) fibers by electrospinning technique. *Journal of Physics: Conference Series*, 2021; **1719 (1)**, 012069.

[40] B He, J Lee and NA Patankar. Contact angle hysteresis on rough hydrophobic surfaces. *Colloids and Surfaces A: Physicochemical and Engineering Aspects*, 2004; **248 (1)**, 101-104.

[41] G Dognani, P Hadi, H Ma, FC Cabrera, AE Job, DLS Agostini and BS Hsiao. Effective chromium removal from water by polyaniline-coated electrospun adsorbent membrane. *Chemical Engineering Journal*, 2019; **372**, 341-351.

[42] M Muratow, F Yalcinkaya, M Bryjak and A Siekierka. Surface-modified PVDF membranes for separation of dye by forward osmosis. *Frontiers in Membrane Science and Technology*, 2024; **3**, 1390727.

[43] P Nuamcharoen, T Kobayashi and P Potiyaraj. Influence of volatile solvents and mixing ratios of binary solvent systems on morphology and performance of electrospun poly(vinylidene fluoride) nanofibers. *Polymer International*, 2021; **70 (10)**, 1465-1477.

[44] D Quéré. Wetting and Roughness. *Annual Review of Materials Research*, 2008; **38 (38)**, 71-99.

[45] D Murakami, H Jinnai and A Takahara. Wetting Transition from the Cassie–Baxter State to the Wenzel State on Textured Polymer Surfaces. *Langmuir*, 2014; **30 (8)**, 2061-2067.

[46] L Jiaoa, K Yana, J Wangb, S Linb, G Lib, F Bic and L Zhang. Low surface energy nanofibrous membrane for enhanced wetting resistance in membrane distillation process. *Desalination*, 2020; **476**, 114210.

[47] J Yuennan, N Tohluebaji, C Putson, N Muensit and P Channuie. Enhanced electroactive β-phase and dielectric properties in P(VDF-HFP) composite flexible films through doping with three calcium chloride salts: CaCl, CaCl·2HO, and CaCl·6HO. *Polymers for Advanced Technologies*, 2024; **35 (6)**, e6437.

[48] S Yempally, P Magadia and D Ponnamma. Effect of Zn-Fe(2)O(3) nanomaterials on the phase separated morphologies of polyvinylidene fluoride piezoelectric nanogenerators. *RSC Advances*, 2023; **13 (48)**, 33863-33874.

[49] SA Salman, FTM Noori and AK Mohammed. Preparation and Characterizations of Poly (vinylidene fluoride) (PVDF) / Ba 0 . 6 Sr 0 . 4 TiO 3 (BST) Nanocomposites. *International Journal of Applied Engineering Research*, 2018; **13 (7)**, 5008-5013.

[50] Z Arifin, S Suyitno, S Hadi and B Sutanto. Improved Performance of Dye-Sensitized Solar Cells with TiO2 Nanoparticles/Zn-Doped TiO2 Hollow Fiber Photoanodes. *Energies*, 2018; **11 (11)**, 2922.

[51] Y Zhou, W Liu, B Tan, C Zhu, Y Ni, L Fang, C Lu and Z Xu. Crystallinity and β Phase Fraction of PVDF in Biaxially Stretched PVDF/PMMA Films. *Polymers (Basel)*, 2021; **13 (7)**, 998.

[52] B Kavitha, KC Sekhar, KS Kumar and N Narsimlu. Influence of NaBr on structural studies of PVA/TiO2 polymer composites. *Optik*, 2023; **272**, 170244.

[53] S Saber, S El-Sayed and AM El Sayed. Influence of Eu3+ on the structural, optical and electrical properties of PEO–PVA: dual bandgap materials for optoelectronic applications. *Journal of Materials Science: Materials in Electronics*, 2023; **34**, 406.

[54] EM Abdallah, TF Qahtan, EM Abdelrazek, GM Asnag and MA Morsi. Enhanced the structural, optical, electrical and magnetic properties of PEO/CMC blend filled with cupper nanoparticles for energy storage and magneto-optical devices. *Optical Materials Part A*, 2022; **134**, 113092.

[55] P Raju, JP Jesuraj and S Muthukumaran. Influence of Ni2+ ions on the structural, morphological, photoluminescence, photo-catalytic and anti-bacterial studies of Cd0.9Zn0.1S nanostructures. *Journal of Materials Science: Materials in Electronics*, 2021; **32**, 14310-14327.

[56] AM Ismail, R Ramadan and MM El-Masry. The role of nanoparticles inclusion in monitoring the physical properties of PVDF. *Journal of the Australian Ceramic Society*, 2023; **59**, 333-341.

[57] L Yesappa, M Niranjana, PS Ashokkumar, H Vijeth, M Basappa, D Jishnu, VC Petwal, S Ganesh and H Devendrappa., Optical properties and ionic conductivity studies of an 8 MeV electron beam irradiated poly(vinylidene fluoride-co-hexafluoropropylene)/ $LiClO_4$ electrolyte film for opto-electronic applications. *RSC Advances*, 2018; **8, 28**.

[58] MAKL Dissanayake, K Umair, GKR Senadeera and JMKW Kumari. Effect of electrolyte conductivity, co-additives and mixed cation iodide salts on efficiency enhancement in dye sensitized solar cells with acetonitrile-free electrolyte. *Journal of Photochemistry and Photobiology A: Chemistry*, 2021; **415**, 113308.

[59] K Mishra, SA Hashmi and DK Rai. Protic ionic liquid-based gel polymer electrolyte: Structural and ion transport studies and its application in proton battery. *Journal of Solid State Electrochemistry*, 2014; bf 18 (8), 2255-2266.

[60] S Lanceros-Méndez, JF Mano, AM Costa and VH Schmidt. FTIR and DSC studies of mechanically deformed beta-PVDF films. *Journal of Macromolecular Science Part B*, 2001; **40 (3-4)**, 517-527.

[61] K Zhang, Z Cui, G Xing, Y Feng and S Meng. Improved performance of dye-sensitized solar cells based on modified kaolin/PVDF-HFP composite gel electrolytes. *RSC Advances*, 2016; **6(102)**, 100079-100089.

[62] A Mayeen, MS Kala, MS Jayalakshmy, JS Thomas, J Philip, D Rouxel, R Bhowmik and N Kalarikkal. Flexible and self-standing nickel ferrite–PVDF-TrFE cast films: promising candidates for high-end magnetoelectric applications. *Dalton Transactions*, 2019; **48 (45)**, 16961-16973.

[63] I Faridmehr, MH Osman, AB Adnan, AF Nejad, R Hodjati and M Azimi. Correlation between Engineering Stress-Strain and True Stress-Strain Curve. *American Journal of Civil Engineering and Architecture*, 2014; **2 (1)**, 53-59.

[64] Anju, RS Yadav, P Pötschke, J Pionteck, B Krause, I Kuritka, J Vilcakova, D Skoda, P Urbánek, M Machovsky, M Masař, M Urbánek, M Jurca, L Kalina and J Havlica. High-Performance, Lightweight, and Flexible Thermoplastic Polyurethane Nanocomposites with Zn^{2+}-Substituted $CoFe_2O_4$ Nanoparticles and Reduced Graphene Oxide as Shielding Materials against Electromagnetic Pollution. *ACS Omega*, 2021; **6 (42)**, 28098-28118.

[65] T He, X Li, Q Wang, Y Zhou, X Wang, Z Wang, N Tavajohi and Z Cui. Poly(vinylidene fluoride) (PVDF) membrane fabrication with an ionic liquid via non-solvent thermally induced phase separation (N-TIPs). *Applied Water Science*, 2022; **12 (3)**, 42.

[66] PI Devi and K Ramachandran. Dielectric studies on hybridised PVDF–ZnO nanocomposites. *Journal of Experimental Nanoscience*, 2011; **6 (3)**, 281-293.

[67] V Elayappan, V Murugadoss, S Angaiah, Z Fei and PJ Dyson. Development of a conjugated polyaniline incorporated electrospun poly(vinylidene fluoride-co-hexafluoropropylene) composite membrane electrolyte for high performance dye-sensitized solar cells. *Journal of Applied Polymer Science*, 2015; **132 (45)**, 42777.

Supplementary

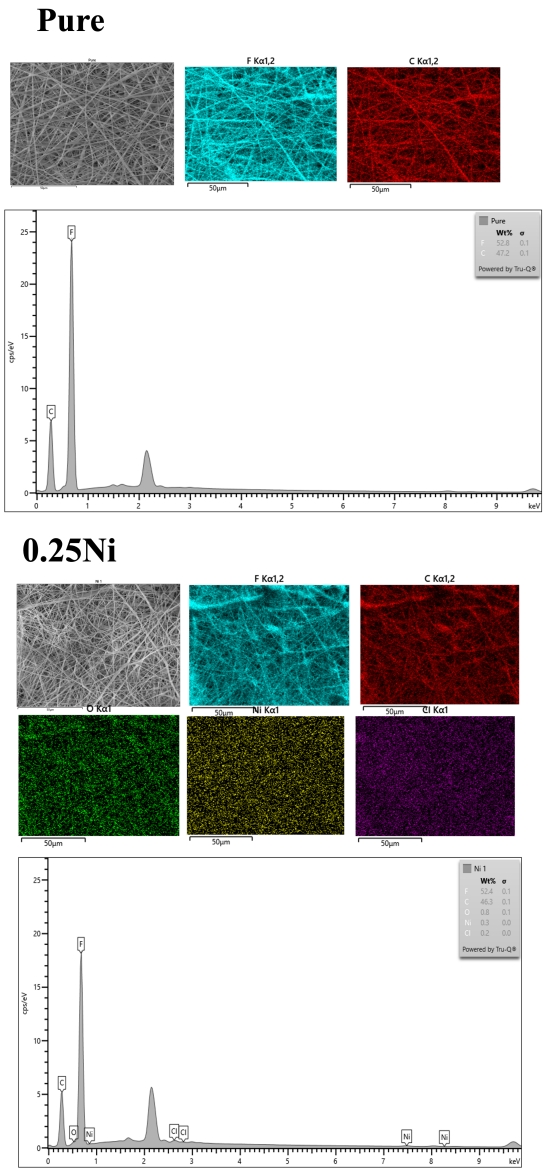

Figure 11: EDS mapping and EDS spectrum components of pristine P(VDF-HFP) and $NiCl_2 \cdot 6H_2O$/P(VDF-HFP) nanofiber mats with varying concentrations of $NiCl_2 \cdot 6H_2O$ shown carbon, fluorine, nickel, oxygen and chlorine distributions in micrographs.

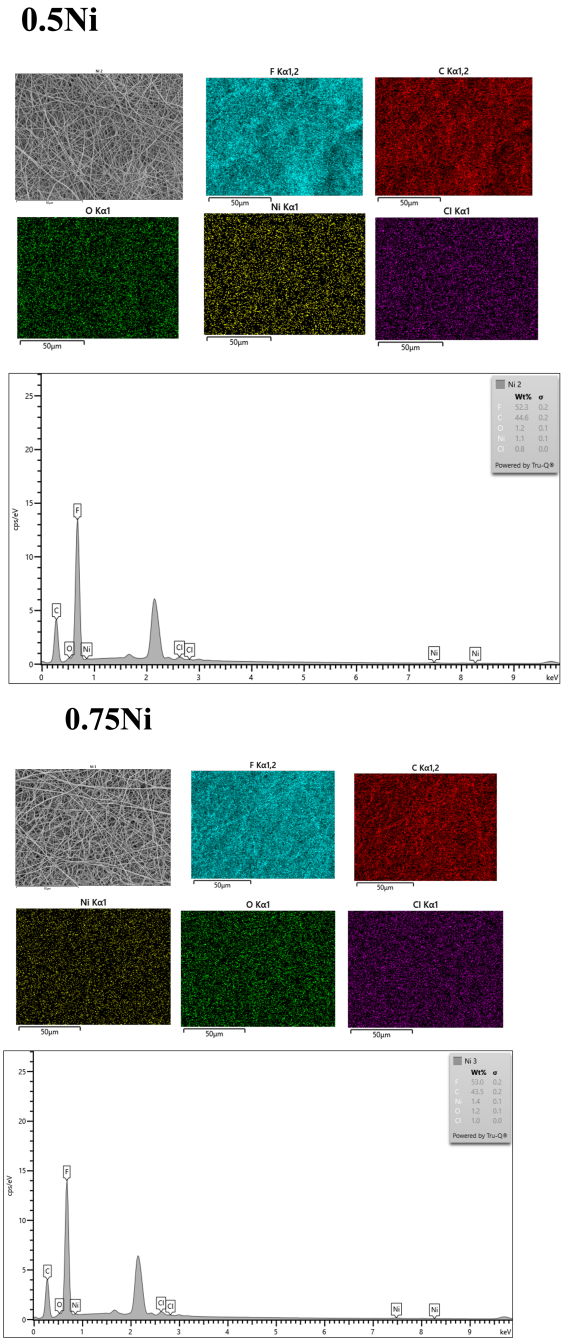

Figure 12: (cont.) EDS mapping and EDS spectrum components of pristine P(VDF-HFP) and $NiCl_2 \cdot 6H_2O$/P(VDF-HFP) nanofiber mats with varying concentrations of $NiCl_2 \cdot 6H_2O$ shown carbon, fluorine, nickel, oxygen and chlorine distributions in micrographs.

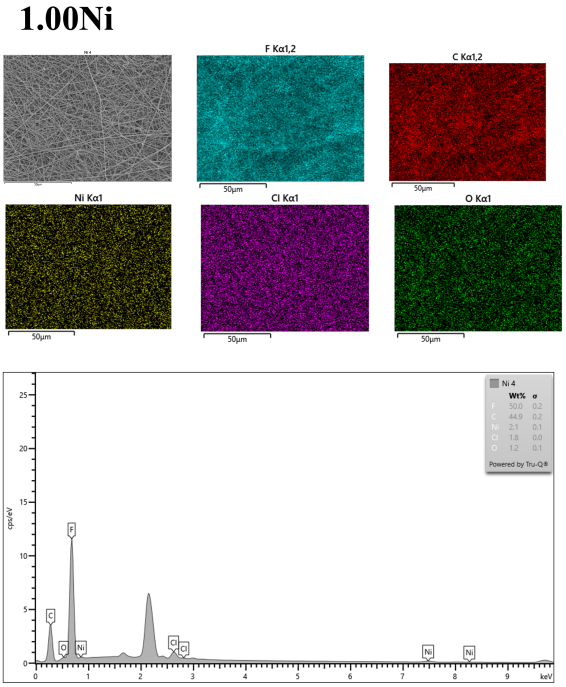

Figure 13: (cont.) EDS mapping and EDS spectrum components of pristine P(VDF-HFP) and $NiCl_2 \cdot 6H_2O$/P(VDF-HFP) nanofiber mats with varying concentrations of $NiCl_2 \cdot 6H_2O$ shown carbon, fluorine, nickel, oxygen and chlorine distributions in micrographs.